LETTER

doi:10.1038/nature15705

Fast-moving features in the debris disk around AU Microscopii

Anthony Boccaletti[1], Christian Thalmann[2], Anne-Marie Lagrange[3,4], Markus Janson[5,6], Jean-Charles Augereau[3,4], Glenn Schneider[7], Julien Milli[4,8], Carol Grady[9], John Debes[10], Maud Langlois[11,12], David Mouillet[3,4], Thomas Henning[6], Carsten Dominik[13], Anne-Lise Maire[14], Jean-Luc Beuzit[3,4], Joseph Carson[6,15], Kjetil Dohlen[12], Natalia Engler[2], Markus Feldt[6], Thierry Fusco[12,16], Christian Ginski[17], Julien H. Girard[4,8], Dean Hines[10], Markus Kasper[4,18], Dimitri Mawet[19], François Ménard[20], Michael R. Meyer[2], Claire Moutou[12], Johan Olofsson[6], Timothy Rodigas[21], Jean-Francois Sauvage[12,16], Joshua Schlieder[6,22], Hans Martin Schmid[2], Massimo Turatto[14], Stephane Udry[23], Farrokh Vakili[24], Arthur Vigan[8,12], Zahed Wahhaj[8,12] & John Wisniewski[25]

In the 1980s, excess infrared emission was discovered around main-sequence stars; subsequent direct-imaging observations revealed orbiting disks of cold dust to be the source[1]. These 'debris disks' were thought to be by-products of planet formation because they often exhibited morphological and brightness asymmetries that may result from gravitational perturbation by planets. This was proved to be true for the β Pictoris system, in which the known planet generates an observable warp in the disk[2–5]. The nearby, young, unusually active late-type star AU Microscopii hosts a well-studied edge-on debris disk; earlier observations in the visible and near-infrared found asymmetric localized structures in the form of intensity variations along the midplane of the disk beyond a distance of 20 astronomical units[6–9]. Here we report high-contrast imaging that reveals a series of five large-scale features in the south-east side of the disk, at projected separations of 10–60 astronomical units, persisting over intervals of 1–4 years. All these features appear to move away from the star at projected speeds of 4–10 kilometres per second, suggesting highly eccentric or unbound trajectories if they are associated with physical entities. The origin, localization, morphology and rapid evolution of these features are difficult to reconcile with current theories.

The system AU Microscopii (AU Mic) is peculiar in many respects. The star is a flaring[10] cool M1Ve type dwarf at a distance of only 9.94 ± 0.13 pc from Earth, and is a member of the β Pic Moving Group, with an age of 23 ± 3 Myr (ref. 11). Its extended (about 200 astronomical units, AU) edge-on, optically thin debris disk was first imaged at visible wavelengths from the ground[12]. The current picture of the system assumes a 'birth ring' of gas-depleted[14] planetesimals located at 35–40 AU (ref. 13). Beyond this radius, the disk is populated by small dust particles (>0.05 μm)[9], probably driven outward by stellar wind; radiation pressure alone would be insufficient to explain the disk's extent[13]. Following the discovery image, the system was intensively observed in 2004/2005 from the ground and space[6–9]. Several intensity inhomogeneities in the form of clumps were reported far from the star at physical separations of 20–40 AU. Most were located in the fainter, southeast side of the disk, while the northwest side was more uniform and approximately twice as bright. The exact positions of these structures differ slightly in the literature, possibly owing to wavelength dependencies[9]. More recently, observations obtained in August 2010 and July 2011 using the Hubble Space Telescope (HST) confirmed the presence of structures in the AU Mic debris disk[15].

AU Mic was one of the prime test targets during the commissioning of SPHERE[16], the planet finder instrument installed at the Very Large Telescope (VLT). It was observed on 10 August 2014, in the J band (1.25 μm) with SPHERE's near-infrared camera IRDIS. Owing to good and stable atmospheric conditions (with seeing about 1.25″ and wind $<10\ \mathrm{m\ s^{-1}}$), the adaptive optics delivered high Strehl ratios (corresponding to 90% to 95% at the SPHERE reference wavelength $\lambda = 1.65$ μm), which resulted in high focal-plane contrasts of 9×10^{-5} at about 0.5″ on average.

The disk is detected out to 7″ (about 70 AU), as limited by the detector field of view, and as close as 0.17″ (about 1.7 AU), below which the disk is attenuated by the coronagraph (Fig. 1). We measured a position angle (PA) of $129.5^\circ \pm 0.3^\circ$ in the southeast side. The northwest-side PA differs by $1.7^\circ \pm 0.4^\circ$ (see Methods). Although the general shape agrees with previous observations, the new SPHERE images show the morphology of the whole disk with unprecedented resolution and detail.

The most striking features revealed by the SPHERE observations are the arch- or wave-like structures close to the star in the southeastern side (annotated A to E in Fig. 1). The features A, B and C, which are located above the midplane, are closer than the ones reported earlier, and do not resemble anything previously observed in circumstellar disks. Two additional fainter structures, D and E, are observed at larger projected separations, closer to and overlapping with the midplane. In addition, they show a wavy (undulating) morphology (Fig. 1). The projected separations of these five structures span the range of ~10 AU to 55 AU (approximately 1.02″, 1.70″, 2.96″, 4.10″ and 5.52″). The typical projected radial extents of the features range between approximately 5 AU (for A, the closest) to 10 AU (for E, the farthest away), and they reach elevations above the disk midplane in the range ~1.5 AU (for

[1]LESIA, Observatoire de Paris, CNRS, Université Paris Diderot, Université Pierre et Marie Curie, 5 place Jules Janssen, 92190 Meudon, France. [2]ETH Zürich, Institute for Astronomy, Wolfgang-Pauli-Strasse 27, CH-8093 Zürich, Switzerland. [3]Université Grenoble Alpes, IPAG, F-38000 Grenoble, France. [4]CNRS, IPAG, F-38000 Grenoble, France. [5]Department of Astronomy, Stockholm University, SE-106 91 Stockholm, Sweden. [6]Max-Planck-Institut für Astronomie, Königstuhl 17, D-69117 Heidelberg, Germany. [7]Steward Observatory, 933 North Cherry Avenue, The University of Arizona, Tucson, Arizona 85721, USA. [8]European Southern Observatory (ESO), Alonso de Córdova 3107, Vitacura, Casilla 19001, Santiago, Chile. [9]Eureka Scientific, 2452 Delmer, Suite 100, Oakland, California 96002, USA. [10]Space Telescope Science Institute, 3700 San Martin Drive, Baltimore, Maryland 21218, USA. [11]Centre de Recherche Astrophysique de Lyon, (CNRS/ENS-L/Université Lyon 1), 9 avenue Charles André, 69561 Saint-Genis-Laval, France. [12]Aix Marseille Université, CNRS, LAM (Laboratoire d'Astrophysique de Marseille) UMR 7326, 13388 Marseille, France. [13]University of Amsterdam, Anton Pannekoek Institute for Astronomy, Science Park 904 1098 XH Amsterdam, The Netherlands. [14]INAF-Osservatorio Astronomico di Padova, Vicolo dell'Osservatorio 5, 35122 Padova, Italy. [15]Department of Physics and Astronomy, College of Charleston, South Carolina, 29424, USA. [16]ONERA—The French Aerospace Laboratory, 92322 Châtillon, France. [17]Sterrewacht Leiden, PO Box 9513, Niels Bohrweg 2, NL-2300RA Leiden, The Netherlands. [18]European Southern Observatory (ESO), Karl Schwarzschild Strasse 2, 85748 Garching bei München, Germany. [19]Department of Astronomy, California Institute of Technology, 1200 East California Boulevard, MC 249-17, Pasadena, California 91125, USA. [20]UMI-FCA, CNRS/INSU France (UMI 3386), and Departamento de Astronomia, Universidad de Chile, Casilla 36-D, Correo Central, Santiago, Chile. [21]Department of Terrestrial Magnetism, Carnegie Institution of Washington, 5241 Broad Branch Road NW, Washington DC 20015, USA. [22]NASA Ames Research Center, Space Science and Astrobiology Division, MS 245-6, Moffett Field, California 94035, USA. [23]Observatoire de Genève, University of Geneva, 51 Chemin des Maillettes, 1290 Versoix, Switzerland. [24]Laboratoire J.-L. Lagrange, Observatoire de la Côte d'Azur (OCA), Université de Nice-Sophia Antipolis (UNS), CNRS, Campus Valrose, 06108 Nice Cedex 2, France. [25]Department of Physics and Astronomy, University of Oklahoma, 440 West Brooks Street, Norman, Oklahoma 73019, USA.

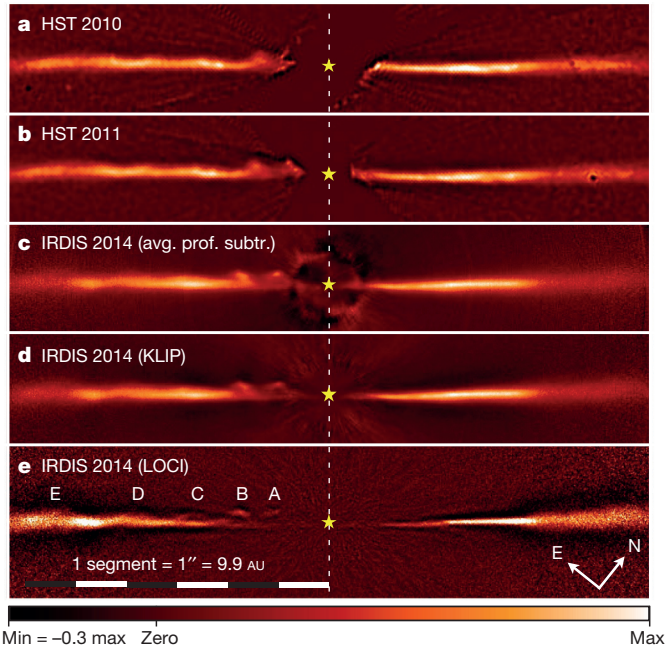

Figure 1 | High-contrast images of the AU Mic debris disk. Images are shown for the three epochs (2010.69, 2011.63 and 2014.69) at the same spatial scale; the location of AU Mic is marked with a yellow star symbol. In **a** and **b**, the HST/STIS data were processed with multi-roll point spread function (PSF)-template subtraction and unsharp mask. SPHERE/IRDIS images are displayed in **c**, **d** and **e**, for three differential imaging techniques (average profile subtraction, KLIP and LOCI) (see Methods). The intensity maps are multiplied by the square of the stellocentric distance to counteract the high dynamic range of the data and to make the disk structures A–E visible at all separations.

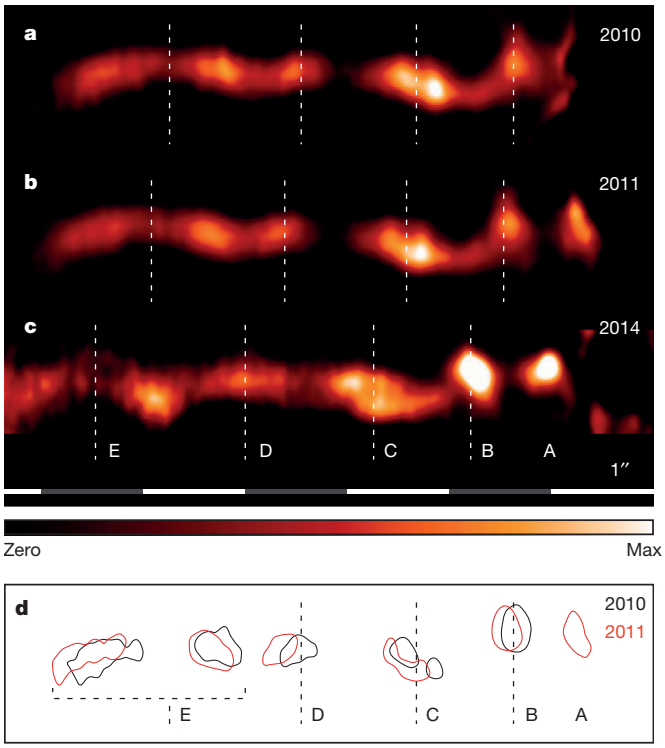

Figure 2 | Extraction of disk substructure from the southeastern side. **a**–**c**, The images from Fig. 1a–c after unsharp masking, subtraction of the smooth main body of the disk, and stretching in the vertical direction by a factor of two (see Methods). The same persistent pattern is recovered in all three epochs, though at shifted locations, implying motion away from the star. **d**, A contour plot of the two HST epochs after more aggressive spatial filtering (Methods), which produces sharp residual features highlighting the differential motion of each feature.

A) to 0.5 AU (for E). Features A and B are recovered with the visible-light instrument channel of SPHERE, as well (Methods).

To confirm the presence and reliability of these features we revisited older observations with HST's Space Telescope Imaging Spectrograph (STIS) in 2010/2011, in which a bump in the midplane was reported in the southeast side at a projected separation of about 13 AU (ref. 15). We reanalysed these data to yield separate images for the 2010 and 2011 epochs, augmented with unsharp masking to render the structures more visible. Both epochs show that this bump is equivalent to the feature B seen in the 2014 SPHERE image but situated about 4 AU closer to the star (Fig. 1), and similarly feature A is also visible from the 2011 epoch. A more careful look reveals that the HST reprocessed images also contain more features all along the midplane. Not only do the features in the SPHERE and HST images match with high fidelity across all three epochs, but they also appear radially offset between epochs, suggesting that the features are moving away from the star, as shown in Fig. 2.

To precisely register the features we plot the disk spine's transversal excursions from the midplane and its intensity as a function of separation from the star (Fig. 3). We note that these two methods do not trace exactly the same physical structures, since the intensity maxima do not coincide with the excursion peaks for the outer features (Fig. 3a, b). Nevertheless, both methods show a persistent pattern shifting away from the star over a 4-year time frame. The five features are clearly identifiable as peaks in the excursion plot. As a general trend, the features get fainter, broader, and closer to the midplane of the disk

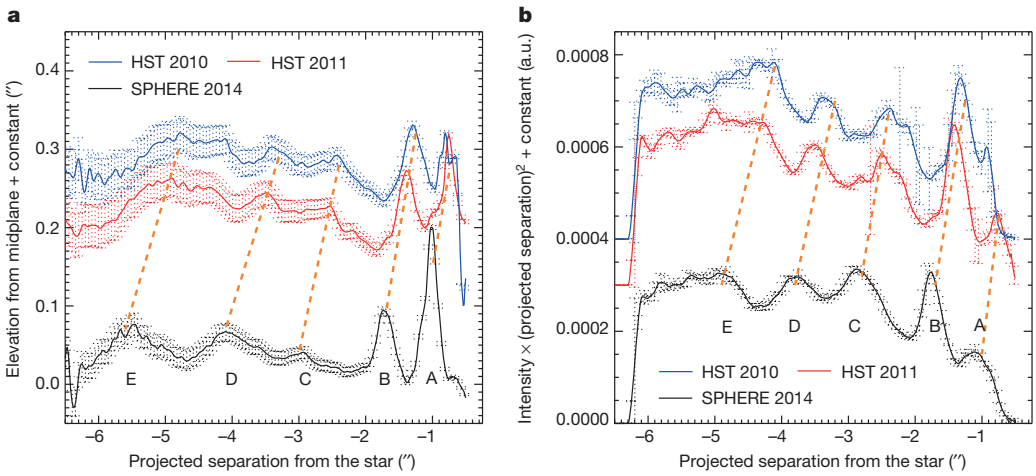

Figure 3 | Disk features across three epochs. Precise registration of the disk spine in the southeast side reveals vertical excursions (**a**) and intensity variations (multiplied by the square of the separation from the star, **b**). The SPHERE profile is an average of three data reductions (ADI, KLIP and subtraction of azimuthally averaged profile). Error bars are 1σ dispersion. The profiles are shifted vertically in proportion to the time intervals between epochs. Disk features are identified as five local maxima (A–E). Dashed orange lines roughly illustrate the possible trajectory of each feature. Feature A is undetected in 2010, being too close to the star. a.u., arbitrary units.

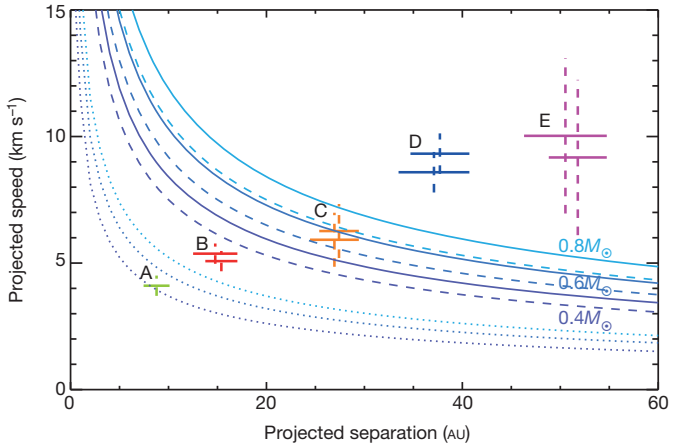

Figure 4 | Projected speeds of the disk features. The projected speeds of the five features A–E (green, red, orange, blue and magenta) are plotted against the projected separation from the star. Several orbits are shown for different mass assumptions (0.4, 0.6 and 0.8 solar masses) and two eccentricities: $e = 0$ (dotted lines), $e = 0.9$ (dashed lines). The solid lines stand for the maximum local system escape speed. Horizontal bars correspond to the range of projected separations between two epochs, while the vertical dotted lines stand for the projected speed uncertainty (peak-to-valley).

with increasing stellocentric distance (Fig. 3). Feature A is inside the blind area of the HST 2010 image. Finally, we conclude that all structures identified in 2014 are recovered in 2010 and 2011 and appear to have moved away from the star towards the southeast direction as a coherent series of patterns. The fact that the two HST epochs alone (biases being minimal) exhibit a noticeable motion is a very strong argument in favour of a real phenomenon. This motion is opposite to that of background objects given AU Mic's proper motion. The colour dependence of the grains' scattering properties cannot account for such a large displacement between the visible and the infrared.

From the three available epochs we obtained the projected speeds associated with each feature considering the excursions from the mid-plane (Fig. 4). To remain conservative the registration errors are peak-to-valley instead of 1σ dispersion. The measured speeds are in the range 4–10 km s^{-1}. Assuming stellar mass in the range of 0.6 ± 0.2 solar masses, the projected speeds of all features beyond A are inconsistent with circular orbits. The speeds of features B and C are compatible with elliptical orbits, but require minimum eccentricities of ~0.5 and ~0.97 even for the high end of the stellar mass range. Features D and E are fainter and less distinct than the closer features, which makes their speed measurements less accurate. However, taking into account the error bars, D and E exceed the local system escape velocity for all stellar mass assumptions. To a lower extent, feature C has a similar behaviour for the lowest-stellar-mass assumption. If confirmed with future measurements, these speeds may indicate that at least two (and possibly three) of the features are on unbound trajectories leaving the system.

Several mechanisms were considered that might produce structures in a dusty disk, some involving a gas-rich disk, spiral waves, resonances with planetary-mass objects, stellar activity, or outflows from planets (see Methods). But the distinct morphology of the features, their high apparent speeds incompatible with low-eccentricity orbits, and their spatial localization on only one side of the disk are at odds with most scenarios. Therefore, we cannot offer a single explanation for these features; additional data are needed to do so. New HST and IRDIS imaging can monitor the morphological, photometric, and astrometric temporal evolution of the features, determine whether their motion slows down or accelerates and whether they expand with time, and possibly observe the generation of new features. Measurements with ZIMPOL, a rapid-switching imaging polarimeter on SPHERE, of scattering polarization can constrain the phase angle and thus the line-of-sight configuration of the features relative to the disk. The Atacama Large Millimeter/submillimeter Array (ALMA) observations can improve constraints on the disk's residual gas content. Monitoring the flaring activity of AU Mic may allow us to test the link between the generation of features in the dust distribution and coronal mass ejections. Finally, Hα differential imaging may reveal signs of accretion if there exist proto-planets in the system.

Online Content Methods, along with any additional Extended Data display items and Source Data, are available in the online version of the paper; references unique to these sections appear only in the online paper.

Received 23 January; accepted 28 August 2015.

1. Smith, B. A. & Terrile, R. J. A circumstellar disk around β Pictoris. *Science* **226,** 1421–1424 (1984).
2. Mouillet, D., Larwood, J. D., Papaloizou, J. C. B. & Lagrange, A. M. A planet on an inclined orbit as an explanation of the warp in the β Pictoris disc. *Mon. Not. R. Astron. Soc.* **292,** 896–904 (1997).
3. Augereau, J. C., Nelson, R. P., Lagrange, A. M., Papaloizou, J. C. B. & Mouillet, D. Dynamical modeling of large scale asymmetries in the β Pictoris dust disk. *Astron. Astrophys.* **370,** 447–455 (2001).
4. Lagrange, A.-M. *et al.* The position of β Pictoris b position relative to the debris disk. *Astron. Astrophys.* **542,** A40 (2012).
5. Nesvold, E. R. & Kuchner, M. J. A SMACK model of colliding planetesimals and dust in the β Pictoris debris disk: thermal radiation and scattered light. Preprint at http://arxiv.org/abs/1506.07187 (2015).
6. Liu, M. C. Substructure in the circumstellar disk around the young star AU Microscopii. *Science* **305,** 1442–1444 (2004).
7. Metchev, S. A., Eisner, J. A., Hillenbrand, L. A. & Wolf, S. Adaptive optics imaging of the AU Microscopii circumstellar disk: evidence for dynamical evolution. *Astrophys. J.* **622,** 451–462 (2005).
8. Krist, J. E. *et al.* Hubble Space Telescope Advanced Camera for Surveys coronagraphic imaging of the AU Microscopii debris disk. *Astron. J.* **129,** 1008–1017 (2005).
9. Fitzgerald, M. P., Kalas, P. G., Duchêne, G., Pinte, C. & Graham, J. R. The AU Microscopii debris disk: multiwavelength imaging and modeling. *Astrophys. J.* **670,** 536–556 (2007).
10. Robinson, R. D., Linsky, J. L., Woodgate, B. E. & Timothy, J. G. Far-ultraviolet observations of flares on the dM0e star AU Microscopii. *Astrophys. J.* **554,** 368–382 (2001).
11. Mamajek, E. E. & Bell, C. P. M. On the age of the β Pictoris moving group. *Mon. Not. R. Astron. Soc.* **445,** 2169–2180 (2014).
12. Kalas, P., Liu, M. C. & Matthews, B. C. Discovery of a large dust disk around the nearby star AU Microscopii. *Science* **303,** 1990–1992 (2004).
13. Augereau, J. C. & Beust, H. On the AU Microscopii debris disk. *Astron. Astrophys.* **455,** 987–999 (2006).
14. Roberge, A., Weinberger, A. J., Redfield, S. & Feldman, P. D. Rapid dissipation of primordial gas from the AU Microscopii debris disk. *Astrophys. J.* **626,** L105–L108 (2005).
15. Schneider, G. *et al.* Probing for exoplanets hiding in dusty debris disks: disk imaging, characterization, and exploration with HST/STIS multi-roll coronagraphy. *Astron. J.* **148,** 59 (2014).
16. Beuzit, J.-L. *et al.* SPHERE: a 'Planet Finder' instrument for the VLT. In *Proc. SPIE Conf. Ser.*, **7014,** 18 (Society of Photo-Optical Instrumentation Engineers, 2008).

Acknowledgements SPHERE was built by a European consortium led by IPAG (France). SPHERE was funded by the ESO, with additional contributions from CNRS, MPIA, INAF, FINES and NOVA. SPHERE also received funding from the European Commission FP6 and FP7 programmes as part of OPTICON under grant numbers RII3-Ct-2004-001566 (FP6), 226604 (FP7) and 312430 (FP7). French co-authors are supported by ANR-14-CE33-0018. Part of this work has been carried out within the framework of the National Centre for Competence in Research PlanetS supported by the Swiss National Science Foundation. C.T. and M.R.M. acknowledge the financial support of the SNSF.This study is based on observations from program 60.A-9249(C) at ESO Very Large Telescope and from program number 12228 made with the NASA/ESA Hubble Space Telescope, obtained at STScI, which is operated by AURA Inc. under NASA contract NAS 5-26555. We are also grateful to the ESO for releasing the commissioning data for publication. Finally, we thank P. Zarka, N. Meyer-Vernet, B. Stelzer and Q. Kral for discussions. J.S. is a NASA Postdoctoral Program Fellow.

Author Contributions A.B. reduced and analysed IRDIS data and wrote the paper. C.T. reduced the IRDIS and ZIMPOL data and contributed to the manuscript writing. A.B., C.T., A.-M.L., M.J., J.-C.A., G.S., C.G., J.D., D.M., T.H., C.D., C.G., J.O. and J.S. worked on the interpretation of the results. G.S., C.G., J.D., D.H., T.R. and J.W. re-reduced HST data. J.M., M.L., D. Mouillet., D. Mawet, J.H.G. and Z.W. operated the instrument at the telescope. A.-L.M. worked on the astrometric calibration. A.B., A.-M.L, M.L., D. Mouillet, T.H., J.-L.B., K.D., M.F., T.F., M.K., F.M., M.M., C.M., J.-F.S, H.M.S, M.T., S.U, F.V. and A.V. contributed to the instrument conception. All authors commented on the manuscript.

Author Information Reprints and permissions information is available at www.nature.com/reprints. The authors declare no competing financial interests. Readers are welcome to comment on the online version of the paper. Correspondence and requests for materials should be addressed to A.B. (anthony.boccaletti@obspm.fr).

METHODS

Observations and data reduction. SPHERE is a highly specialized instrument dedicated to high-contrast imaging, built by a wide consortium of European laboratories and recently installed at the VLT[16]. It is based on the Sphere Adaptive optics for eXoplanet Observation (SAXO) extreme adaptive optics system, with a 41×41 actuator wavefront control. Several coronagraphic devices for stellar diffraction suppression are provided, including apodized Lyot coronagraphs.

AU Mic was observed on 11 August 2014, with the differential imaging camera IRDIS, in the J band for a total integration time of 2,560 s. IRDIS offers two square fields of view (about 12″ each) on the same detector to allow for spectral differential imaging, but since the broadband J filter was used for both channels, they provided redundancy in this case. The star was masked with an apodized Lyot coronagraph of which the focal mask occults an area of 185 mas in diameter and the pupil mask transmits ~67% of the light.

Data reduction follows a standard procedure including cosmetics (correction for flat-field, bad pixels, dark current, and distortion). Individual frame registration is not required as the sequence is very stable and a dedicated hardware in SPHERE is taking care of the positioning of the star onto the coronagraph in real time, reaching 0.5 mas accuracy[17].

We then took advantage of the field rotation during the observation (~77°) to suppress the residual starlight in coronagraphic images and reveal the faint scattered light from the debris disk via angular differential imaging (ADI). We explored several ADI techniques, including classical ADI, LOCI[18] and KLIP[19] with various parameter settings. The final images were obtained with a LOCI (Fig. 1e) frame selection criterion of 0.75 full-width at half-maximum (FWHM), and an optimization zone of 10,000 PSF footprints (using sectors of annuli 12 FWHM in the radial dimension), while the KLIP image (Fig. 1d) is calculated for separations shorter than 600 pixels (7.35″), and is built from the subtraction of 5 modes out of 160 (a conservative value to avoid strong attenuation of the disk). Since ADI techniques achieve their high contrast performance at the cost of flux losses to the disk image, which remain difficult to calibrate[20], we also reduced the data with less powerful but more conservative methods, such as frame-by-frame reference star subtraction or subtraction of an azimuthally averaged radial profile. Owing to the high quality and stability of the data, these methods performed similarly to the ADI techniques in terms of detecting the disk at separations larger than ~0.7–1.0″. Doing so, the processed images reach a 5σ contrast as large as 4×10^{-6} at ~0.5″. All data reduction methods recover the disk features A–E consistently and at the same locations.

The limit of detection to point sources is presented in Extended Data Fig. 1, as measured within the disk using the method of fake point sources injection to calibrate for the self-subtraction inherent to ADI. The contrast achieved in the image at a projected separation of 1″ would have enabled the detection of a planet with a mass 1 to 6 times that of Jupiter, depending which evolutionary and atmospheric model is considered[21,22], and assuming an age of 20 Myr. This threshold potentially lowers to a Saturn-mass object at a projected separation of 4″ (about the location of the planetesimal belt), but the models are not reliable for such low mass.

The published images of the optical HST observations from 2010 and 2011 represent a combination of both epochs[15], in which the strongest feature (B) was already identified. For the purpose of tracking our disk features A–E through time, these data were re-reduced to yield separate images for both epochs. Following the original recipe for data reduction (multi-roll PSF-template subtraction) augmented with an additional high-pass filtering (unsharp masking), we recover features B–E reliably in both epochs. In 2010, feature A resides inside the blind area resulting from the multi-roll technique. The HST images are obtained with STIS in a filter-less mode, the spectral range being set by the detector spectral response across a very broad band (200–1,100 nm).

For Figs 2a–c, the images shown in Fig. 1a–c were unsharp-masked on a spatial scale of 0.76″. The main body of the disk was approximated as a brightness distribution with a broken linear horizontal profile (with a break at 3″, the approximate radius of the source ring) and a Gaussian vertical profile. The linear trends were chosen on the basis of the disk's brightness profile along the midplane. This distribution was subtracted to reveal the inhomogeneous substructure. The same distribution was used for both HST epochs, preserving their extreme reliability. In Fig. 2d, a more aggressive asymmetric kernel of $0.76'' \times 0.25''$ was used for unsharp-masking on the two HST images to highlight sharp horizontal gradients that are suitable for visualizing the differential motion.

On 13 August 2014, we obtained a follow-up observation of AU Mic with ZIMPOL, the rapid-switching imaging polarimeter. A total of 1 h of integration time was taken in the I′-band filter (713–866 nm) in imaging mode (no polarimetry) with pupil tracking so as to allow for ADI data reduction. Since the high-sensitivity detector mode is currently only available in the slow polarimetry mode, which does not support pupil tracking, the noisier high-gain detector mode was used. AU Mic was heavily saturated and produced some charge bleeding in the vertical direction, but the compromised region does not affect the disk detection. A total of 40° of field rotation was captured during the observation. After correcting for cosmetics as for the IRDIS data, we applied various ADI data reduction techniques to suppress the stellar halo. In Extended Data Fig. 2, we show the results for LOCI data reduction with 'conservative' parameter settings[23] including a frame selection criterion of $0.5 \times$ FWHM and an optimization area of 10,000 PSF footprints (same geometry as for IRDIS). The adaptive optics correction is more difficult at shorter wavelengths, and thus yields a lower Strehl ratio in the optical than in the infrared. On the other hand, the shorter wavelengths yield a higher angular resolution ($\lambda/D \approx 19$ mas in the I′-band as compared to about 32 mas in the J-band) and thus a greater potential to resolve fine structure. As Extended Data Fig. 2 demonstrates, the location and overall morphology of the A and B features as seen in the IRDIS images are very well reproduced in the ZIMPOL images, including the wave-like connection of feature A to the disk plane. Both images show an additional pattern in between feature B and the midplane. This structure may represent further wave-like features like A–E at a lower amplitude, but will require future investigation and modelling.

Disk morphology. From a morphological point of view, the southeast and northwest sides of the disk are very different. The former contains many structures above the midplane, while the latter is brighter, thinner and features an abrupt change of direction near 1.5″. The disk PA, measured from north to east, is determined in both SPHERE and HST images using the method developed earlier for edge-on disks[4]. The image is rotated with an initial guess for the PA to place the disk midplane approximately horizontally and a profile function (Gaussian or Lorentzian) is fitted vertically to retrieve the midplane centroid versus the angular separation. We used regions where the disk contains as few features as possible (3″ to 6″ here). The true disk PA is the image rotation for which the slope of the disk centroid is flat. The measurement is repeated separately for the two sides, since the AU Mic disk is highly asymmetric. We found $PA_{SE} = 129.5 \pm 0.2°$ and $PA_{NW} = 311.2 \pm 0.3°$ respectively for the southeast and northwest sides. Similarly in the HST images we obtained $PA_{SE} = 129.0 \pm 0.5°$ and $PA_{NW} = 310.5 \pm 0.2°$. Although the error is relatively large, the measurements from SPHERE and HST differ in the northwest side by $0.7 \pm 0.4°$. We suspect that the determination of the PA in the southeast is in fact perturbed by the presence of the features appearing at different locations between 2010–2011 and 2014. Thus, we considered that the northwest side gives a more reliable measurement of PA so we compensated the HST image with a rotation of 0.7° to realign all the epochs. We note that for both HST and SPHERE the true north uncertainty is ~0.1°, so the uncertainty on the disk PA is reflecting our ability to locate the disk midplane and is also possibly affected by the colour dependence of the grains. In addition, the two sides are clearly misaligned by $1.7 \pm 0.4°$ in the SPHERE image and by $1.5 \pm 0.5°$ in the HST image. Once the disk PA is set, the centroid of the disk cross-section versus separation defines the disk spine in which the features are visible as excursions from the midplane (Extended Data Fig. 3). This spine includes both the main disk and the features, which explains that they may appear in Extended Data Fig. 3 at different elevations than in Fig. 1. To register the radial locations of features we used a model profile combining a Gaussian and a first-order polynomial in some delimited regions (red lines in Extended Data Fig. 3). The measurement is repeated for various data reductions, including PA uncertainty, to estimate the errors on the location of the features. The registration of features and associated errors are listed in Extended Data Table 1.

Finally, we also found that the disk spine shows an excursion of 0.07″ (equivalent to ~5–6 pixels) southwest to the star inside a radius of 0.6–0.7″, a characteristic that is clearly seen in a zoomed image (Extended Data Fig. 4). It is unlikely to be a result of ADI bias, which is expected to be symmetrical about the disk midplane. Similar excursions were observed in a number of debris disks; these excursions could represent the opening of each disk's source ring as viewed at an inclination close to, but not equal to, 90°. In such a situation, anisotropic forward-scattering is expected to render the near-side edge of the ring much brighter than the far-side edge, which accounts for the asymmetry. A complete analysis of the disk photometry is deferred to future work, since a careful modelling of ADI bias effects is crucial in that case, especially close to the star[20].

With the most aggressive algorithms (those that remove the starlight most efficiently, like KLIP and LOCI) the three features closest to the star appear as arches; that is, the structures are clearly separated from the midplane by a void of scattered light. As a qualitative 'sanity check', fake bumps were added to the data inside the disk midplane to investigate qualitatively whether ADI could produce a depletion between the midplane and the top of the bump, mimicking arches. We found no such effects and therefore conclude that this is probably a real characteristic, to be confirmed with deeper follow-up observations.

As a complement to Figs 3 and 4, we have plotted the stellocentric distance versus time for each feature in Extended Data Fig. 5. The structures are well aligned

over the three epochs, error bars being smaller than the plotted symbols in some cases. Once the data points are fitted with linear trends and extended back in time, three out of five features (A, B, C) lie on nearly parallel tracks, and suggest a timeframe of ~15 years (where lines intersect the *y* axis). In fact, the observed structures are necessarily recent, otherwise they would have propagated and smeared all around the star as a result of secular evolution. Brightness asymmetries reported in the literature in 2004 may coincide with the tracks for features C and D, though it is difficult to determine reliably whether they are the same features since they are seen as intensity variations rather than excursions from the midplane.

Physical interpretation of disk features. A majority of known debris disks exhibit structural features such as eccentricities, warps and brightness asymmetries, which are assumed to be induced by planets via secular gravitational perturbation. However, such features either appear static over observational timescales or remain coupled to the Keplerian motion of the disk, which is incompatible with the fast motion measured for two or three of the five features observed. There are mandatory observational facts with which a physical interpretation must comply, at least qualitatively, which are: (1) spatial localization of the features on one side of the disk and above the midplane, (2) timeframe for the evolution, (3) increase of projected speeds at larger projected separations, (4) larger projected radial widths away from the star, (5) increase of intensities at shorter projected separations, and (6) variable elevations.

Although a number of mechanisms occur in massive protoplanetary disks that can affect the dust distribution and generate structures with speeds of a few to a few tens of kilometres per second, they rely on the presence of gas. Although some debris disks retain a large amount of gas[24], such gas is probably a low-mass component in the AU Mic system[14] compared to the estimated total mass of dust[9]. For these reasons gas-induced scenarios (such as radiation-driven disk wind and protostellar jets) are considered unlikely here.

One possible assumption would be that the measured speeds represent the phase speed of a pattern propagating through the disk, which could greatly exceed the physical speed of the constituent disk particles. Indeed, protoplanetary disks may exhibit spiral density waves whose outer arms 'travel' at super-Keplerian speeds, as a response to gravitational instabilities or planets orbiting inside the disk[25]. Given AU Mic's youth, it must have dispersed its primordial gas only recently; thus, some disk structures could conceivably have survived as 'fossils'. Whether this is physically plausible remains to be investigated. Resonances can induce wave-like structure even in gas-less disks. Saturn's rings feature edge waves along the orbits of embedded moons, although they follow Keplerian orbits[26]. Lindblad resonances, on the other hand, produce spirals phase-locked to a planet, which exhibit super-Keplerian phase speeds. However, a spiral would have to 'wrap' around the star several times to reproduce the observed train of features on the southeastern side, which is at odds with the lack of features on the northwestern side.

Local intensity enhancements on one side only could be interpreted as a series of concentric eccentric rings resulting from massive collisions of asteroid-like objects[27]. However, the typical timescale to produce several eccentric rings is of the order of 100 years, too long compared to our measurements for the moving structures in the AU Mic disk.

Rather than phase speed, the observed motion may represent physical motion at super-Keplerian velocities. Dust blowout by stellar radiation or wind constitutes an integral part of the mechanism that produces debris disks, and is well capable of boosting small grains to escape speeds. Given AU Mic's high activity level, flares from coronal mass ejections could occasionally impact the planetesimal ring and produce distinct dust clouds at different azimuths. A warped ring of planetesimals as in β Pictoris[5] could account for the elevation. Owing to anisotropic scattering, the near-side clouds could appear bright while those on the far side remain undetected, explaining the one-sided apparent distribution. Similarly, the interaction of episodic flares with a planet's magnetosphere or a dusty circumplanetary disk, on a Keplerian orbit, may explain the spatial localization of the features as a train of dust cloud[28]. Circumplanetary disks are also capable of releasing outflows[29]. In both of these scenarios, the combination of orbital motion of the dust source and the outward force would explain the velocity dispersion shown in Fig. 4.

In the planetary outflow scenario, given that features A and E could have been released approximately 15 years apart (Extended Data Fig. 5) and that projected speeds vary from ~4 km s^{-1} to 10 km s^{-1}, we can constrain the minimal separation of a planet to ~10–15 AU. On the other hand, dust clearing observed at distances closer than ~35–40 AU could be the result of a planet orbiting inside the planetesimal belt. Therefore, in the range 10–40 AU, where a hypothetical planet may reside, the SPHERE data reach a contrast of 1×10^{-6} to 8×10^{-8}, which, for the DUSTY model[21], provides an upper limit at 6 and 3.5 Jupiter masses, respectively.

Code availability. Data reductions are performed with IDL and custom routines (including IDP3 available from the Mikulski Archive for Space Telescopes at STScI).

17. Baudoz, P. *et al.* The differential tip-tilt sensor of SPHERE. In *Proc. SPIE Conf. Ser*, **7735,** 5 (Society of Photo-Optical Instrumentation Engineers, 2010).
18. Lafrenière, D., Marois, C., Doyon, R., Nadeau, D. & Artigau, E. A new algorithm for point-spread function subtraction in high-contrast imaging: a demonstration with angular differential imaging. *Astrophys. J.* **660,** 770–780 (2007).
19. Soummer, R., Pueyo, L. & Larkin, J. Detection and characterization of exoplanets and disks using projections on Karhunen-Loève eigenimages. *Astrophys. J.* **755,** L28 (2012).
20. Milli, J. *et al.* Impact of angular differential imaging on circumstellar disk images. *Astron. Astrophys.* **545,** A111 (2012).
21. Chabrier, G., Baraffe, I., Allard, F. & Hauschildt, P. Evolutionary models for very low-mass stars and brown dwarfs with dusty atmospheres. *Astrophys. J.* **542,** 464–472 (2000).
22. Baraffe, I., Chabrier, G., Barman, T. S., Allard, F. & Hauschildt, P. H. Evolutionary models for cool brown dwarfs and extrasolar giant planets. The case of HD 209458. *Astron. Astrophys.* **402,** 701–712 (2003).
23. Thalmann, C. *et al.* Imaging of a transitional disk gap in reflected light: indications of planet formation around the young solar analog LkCa 15. *Astrophys. J.* **718,** L87–L91 (2010).
24. Moór, A. *et al.* ALMA continuum observations of a 30 Myr old gaseous debris disk around HD 21997. *Astrophys. J.* **777,** L25 (2013).
25. Muto, T. The structure of a self-gravitating protoplanetary disk and its implications for direct imaging observations. *Astrophys. J.* **739,** 10 (2011).
26. Weiss, J. W., Porco, C. C. & Tiscareno, M. S. Ring edge waves and the masses of nearby satellites. *Astron. J.* **138,** 272–286 (2009).
27. Kral, Q., Thébault, P., Augereau, J. C., Boccaletti, A. & Charnoz, S. Signatures of massive collisions in debris discs. A self-consistent numerical model. *Astron. Astrophys.* **573,** A39 (2015).
28. Kivelson, M. G. & Southwood, D. J. Dynamical consequences of two modes of centrifugal instability in Jupiter's outer magnetosphere. *J. Geophys. Res.* **110,** A12209 (2005).
29. Fendt, C. Magnetically driven outflows from Jovian circum-planetary accretion disks. *Astron. Astrophys.* **411,** 623–635 (2003).

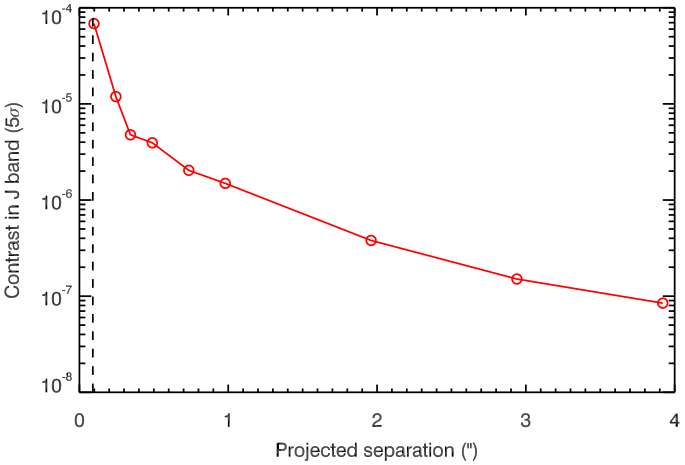

Extended Data Figure 1 | Limit of detection to point sources. The contrast is measured at 5σ using fake planets introduced to the data at discrete positions (circles) along the disk midplane to account for the self-subtraction of the ADI/KLIP algorithm. The dashed line defines the edge of the coronagraphic mask at 0.09″.

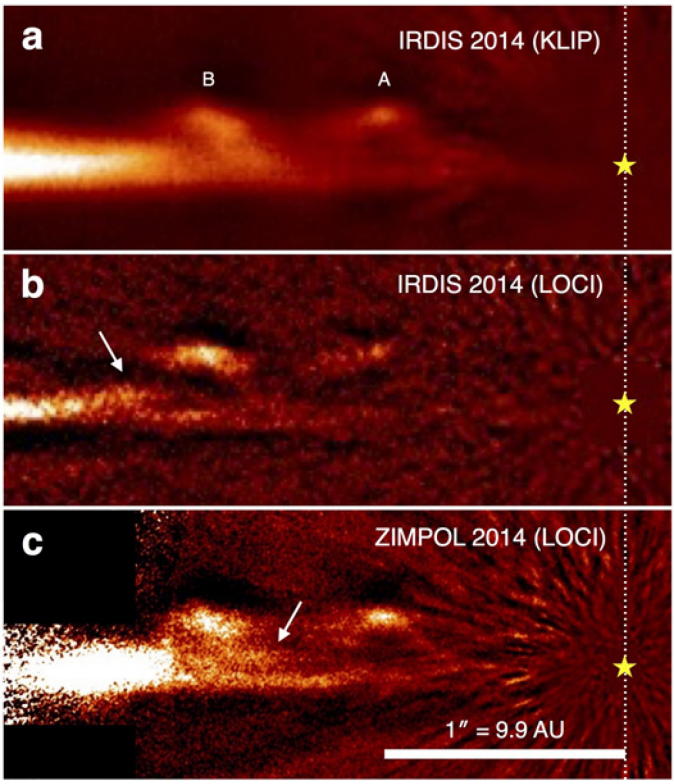

Extended Data Figure 2 | Comparison of IRDIS and ZIMPOL images. **a** and **b** show zoomed-in regions of the KLIP and LOCI reductions of the IRDIS infrared data, whereas **c** is taken from the conservative LOCI reduction of the ZIMPOL optical data. Features A and B are reproduced accurately in the ZIMPOL data. An additional substructure between feature B and the midplane is also detected, as indicated by arrows. The yellow star symbol indicates the position of the star.

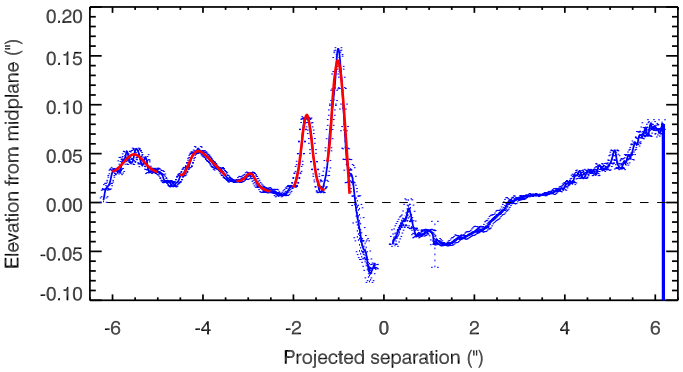

Extended Data Figure 3 | Spine of the disk measured in SPHERE IRDIS data. The spine is measured using several reductions (noADI, ADI, KLIP) of the SPHERE IRDIS 2014 data. Average values and dispersions (error bars) are plotted as a blue line. For each region where a local maxima is identified, a Gaussian + first-order polynomial model is fitted in order to register precisely the five features.

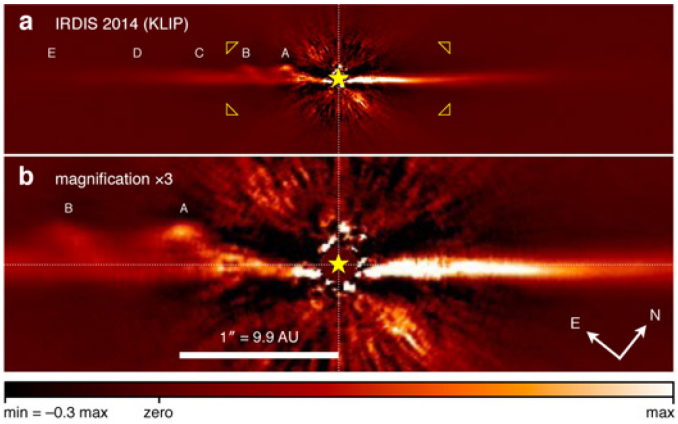

Extended Data Figure 4 | Central part of the SPHERE IRDIS image. **a** shows a 12″ field of view of the SPHERE IRDIS image processed with the KLIP algorithm and **b** is a magnified version to indicate the bow-like deviation of the disk to the southeast in the central area (for separations shorter than ~0.7″). The horizontal dotted lines indicate the disk midplane.

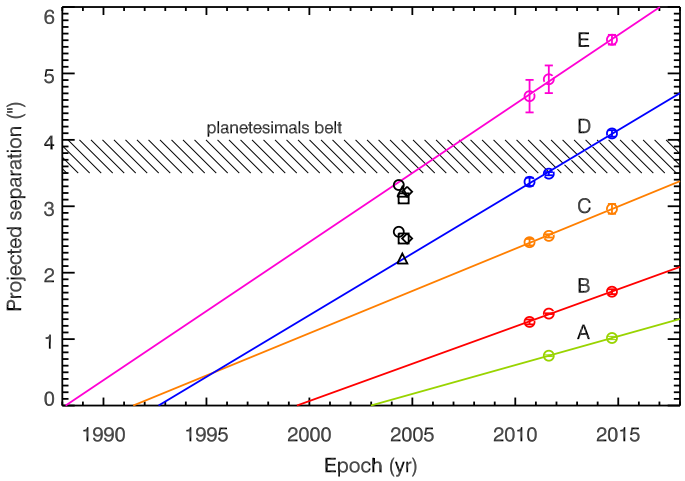

Extended Data Figure 5 | Positions of the disk features over time. The positions of the features measured in the SPHERE and HST images are plotted as circles together with peak-to-valley error bars (in some cases, the errors are smaller than the symbol size). Linear fits on these three epochs illustrate the possible track of each feature. The black symbols show the location at which various inhomogeneities were reported in the literature, on the basis of older data[6–9]. The colour coding is the same as in Fig. 4.

Extended Data Table 1 | Registration of features

Epoch	feature A	feature B	feature C	feature D	feature E
2010 HST	–	1.259 ± 0.037″	2.459 ± 0.049″	3.369 ± 0.061″	4.658 ± 0.245″
2011 HST	0.750 ± 0.012″	1.384 ± 0.012″	2.554 ± 0.025″	3.491 ± 0.025″	4.912 ± 0.208″
2014 SPHERE	1.017 ± 0.025″	1.714 ± 0.037″	2.961 ± 0.073″	4.096 ± 0.049″	5.508 ± 0.074″